Effect of gravity in wheel/terrain interaction models

László L. Kovács, Bahareh Ghotbi, Francisco González, Parna Niksirat, Krzysztof Skonieczny, József Kövecses

This is the peer reviewed version of the following article:
Effect of Gravity in Wheel/Terrain Interaction Models, L. Kovács, B. Ghotbi, F. González, P. Niksirat, K. Skonieczny, J. Kövecses, Journal of Field Robotics 37(5):754–767, 2020,
which has been published in final form at https://doi.org/10.1002/rob.21924.

Abstract

Predicting the motion of wheeled robots in unstructured environments is an important and challenging problem. The study of planetary exploration rovers on soft terrain introduces the additional need to consider the effect of non-terrestrial gravitational fields on the forces and torques developed at the wheel/terrain interface. Simply reducing the wheel load under earth gravity overestimates the travelled distance and predicts better performance than is actually observed in reduced-gravity measurements. In this paper, we study the effect of gravity on wheel/terrain interaction. Experiments were conducted to assess the effect of reduced gravity on the velocity profile of the soil under the wheel, as well as on the traction force and sinkage developed by the wheel. It was shown that in the velocity field of the soil, the decay of the tangential velocity component becomes gradual with reducing gravity, and the decay of the normal to rim velocity is slower in Lunar gravity. It was also found

that wheel flexibility can have an important effect on the dynamics as the contact patch and effective radius varies periodically. These results were then used together with traditional semi-empirical terramechanics models to determine and validate the simulated drawbar pull values. The developed simulation model includes the effect of wheel flexibility, dynamic sinkage and gravity.
Keywords: Modelling and simulation, Reduced gravity experiment, Velocity field, Wheel flexibility, Wheel-soil interaction.

1 Introduction

One of the key challenges for planetary rovers is testing in representative environments here on Earth. Field testing in analogue terrains helps to understand the mobility of a rover and its guidance, navigation, and control capabilities. However, no perfect analogue can be achieved, meaning that field tests must still be supplemented with other forms of testing.

It is commonplace to perform mobility field tests for Mars rovers with reduced-mass engineering models to mimic the wheel loads that will be experienced in the reduced gravity environment of Mars. For example, SSTB-lite and Scarecrow are 3/8 mass versions of the Mars Exploration Rovers (Opportunity and Spirit) and Mars Science Laboratory rover (Curiosity), respectively [17, 13]. Although these tests correctly capture the effect of reduced gravity (and thus weight) on wheel loads, they do not capture the effect that gravity has on the granular material itself.

Flights aboard aircraft flying parabolic arcs are the best opportunity to achieve significant stretches of effectively reduced gravity in a controlled fashion without actually travelling to extraterrestrial surfaces. Only a single dataset had been described in the literature before for wheel-soil interaction during reduced-g flights: the work of Kobayashi et. al. This dataset is based on a self-propelled rigid wheel driving in FJS-1 lunar soil simulant and in Toyoura sand in a wide range of gravity conditions: 1/6 g, 1/2 g, 3/4 g, 1 g, and 2 g. The data collected includes horizontal travel distance, vertical sinkage, and wheel torque. The data is contrasted to a dataset collected in 1 g that is corresponding but with varying vertical load on the wheel (i.e. 1/6 W, 1/2 W, etc.). The difference between the experimental conditions in the two datasets is the effect of gravity on the soil particles themselves. The key observation in [16] is that wheel mobility can be reduced when both the wheel and soil are in reduced gravity, rather than improving as

it does when just the load on the wheel is reduced. Another observation, which may in fact contribute to the first, is that wheel sinkage is not affected significantly when a constant mass wheel is driven in differing gravity conditions.

Wong proposed a terramechanics formulation in [31] that uses a pressure-sinkage coefficient that is proportional to the gravitational acceleration to consider different values, and concluded that such a formulation can account for the sinkage and compaction resistance (assumed proportional to wheel torque for a self-propelled wheel) data presented in [16].

This paper extends the work of both Kobayashi et. al. and Wong. New reduced-gravity wheel-soil interaction data is used here. The dataset goes further than the one presented in [16] by executing slip-controlled experiments with a flexible wheel and explicitly measuring resulting drawbar pull (i.e., net traction force).

The main focus and contribution of this work lie in the incorporation of the observed gravity effects in the terramechanics modeling and simulation. This includes the computation of predicted drawbar pull to compare against the experimental results. To achieve this, the formulation is augmented with an approach proposed in [8] to consider dynamic sinkage, as well as a novel approach to account for a periodically varying contact patch between the flexible wheel and the soil.

The remainder of this article is organized as follows. First, in Section 2, the experimental system and the conditions at which the velocity fields of soil under the wheel and the drawbar pull measurements were conducted is described. Then, in Section 3, a surrogate wheel model is developed based on the analysis of recorded high-speed camera images, and a detailed velocity field study is carried out in order to determine the effect of gravity on the soil motion under the wheel. Section 4, presents the dynamic model which incorporates wheel flexibility, slip sinkage and the effect of gravity. The simulation results are compared to experiments in Section 5, while Section 6 concludes the paper.

2 Reduced gravity experiments

2.1 Automated terramechanics robotic system

The main experimental apparatus consists of a sandbox beneath a robotic gantry that drives a wheel through the soil in the box (Fig. 1). The gantry consists of a linear actuator that advances the wheel horizontally, a motor that turns the wheel, and pneumatic actuators that apply a downward force on the wheel. By these mechanisms, the slip rate and normal force of the wheel are controlled. A prototype wheel of the ExoMars rover reported in [19, 22] was used in the experiments. It is flexible and compliant with a 285 mm diameter, 120.8 mm width and 12 grousers. The wheel radial stiffness at the operating load range of 130 N to 200 N varies depending on the wheel position in contact with the ground. On average, at positions "midway-between-springs" the local stiffness is 37.3 N/mm with radial displacement from 23.5 mm to 25.5 mm. At positions "center-on-spring" the local stiffness is 11.2 N/mm with radial displacement from 12.3 mm to 18.5 mm. The rover wheel is driven (via synchroanized control of a horizontal linear actuator and a wheel motor) in an instrumented sandbox testbed that measures 6-axis force/torque components along with wheel sinkage. The wheel is pressed up against a transparent 780×200 mm window on the sidewall of the sandbox, and a high-speed camera observes wheel-soil interactions through this window (via a mirror reflection for the sake of system compactness). By keeping the rotational velocity constant and changing the translational velocity during each parabola certain slip values were targeted. The experiments described above flew aboard a Falcon 20 aircraft of the National Research Council of Canada (NRC) . Highspeed images were collected at Lunar and Martian gravities and compared with the on-ground experiments in 1-g to understand the effect of partial gravity on the wheel-soil interactions.

2.2 Reduced-gravity flight campaign

Reduced gravity wheel-soil experiments are divided between Martian and Lunar gravity parabolas (seven Lunar-g parabolas, and ten Martian-g parabolas). These experiments are referred to as partial gravity experiments (PGE), in contrast to 1-g on-ground experiments (OGE). Testing the ExoMars wheel in Martian gravity is directly relevant to the upcoming ExoMars mission. Experiments at lunar gravity present a clear contrast to 1-g, providing a valuable boundary case for developing planetary and reduced-g terramechanics models. Three sets of tests were executed

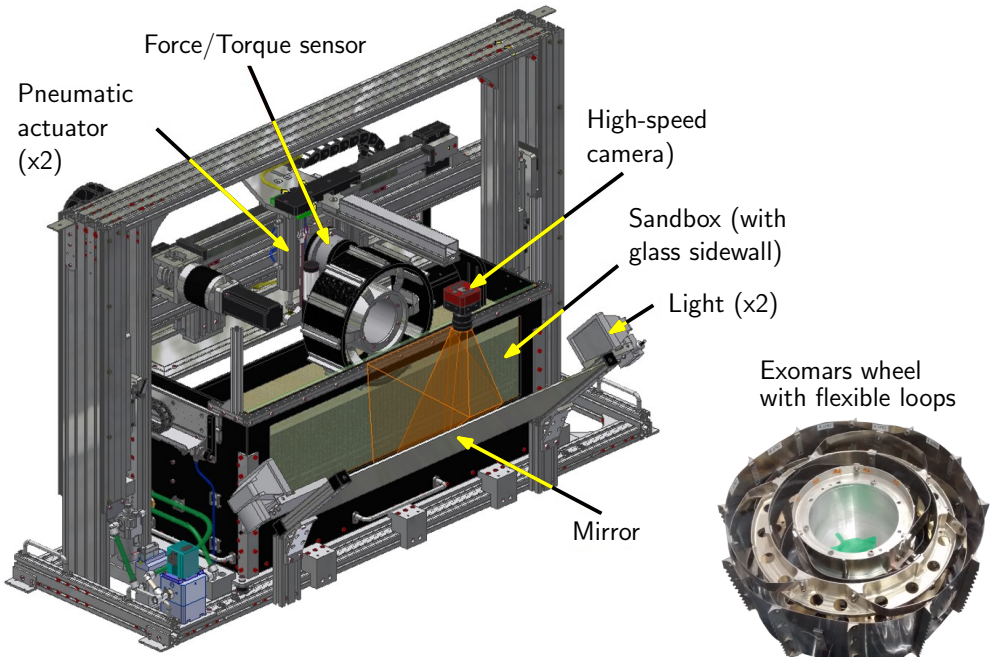

Figure 1: Automated experimental apparatus for performing slip-controlled wheel experiments during reduced-g parabolas. The configuration shown includes a 28.5 cm diameter wheel and 80 kg of ES-2 Martian soil simulant. The camera field of view moves with the wheel unit.

at 20% slip in both Martian and Lunar-g, for analysis of repeatability, and all other conditions were tested once.

The key elements of reduced-gravity flights are the preparation phase and the reduced-g parabola. After instrumentation preparation, the aircraft descends and then executes a 2-g pull up after which it transitions into approximately 20-25 seconds of reduced-gravity. Following the parabola, the aircraft pulls out in another 2-g manoeuvre and then returns to preparation phase altitude (see Fig.2). The two key functions of a reduced-gravity terramechanics testing system correspond to the two key elements of the reduced-g flight trajectory; one is the test execution and data collection (performed in reduced-g parabola) and the other is soil preparation (performed in preparation phases between reduced-g parabolas).

A rapid automated soil preparation system was developed to provide repeatable test conditions. It has the capability to perform consistently repeatable soil preparation in under 15 seconds while satisfying the many constraints and requirements stemming from operating on-board a reduced-gravity flight aircraft. The solution developed for this involves elements of blowing jets of compressed air (for loosening) and vibration (for levelling and compaction). The concept for the soil preparation was introduced by the authors in reference [26] and the detailed design and repeatability analysis is given in reference [27]. The system is the first of its kind to be au-

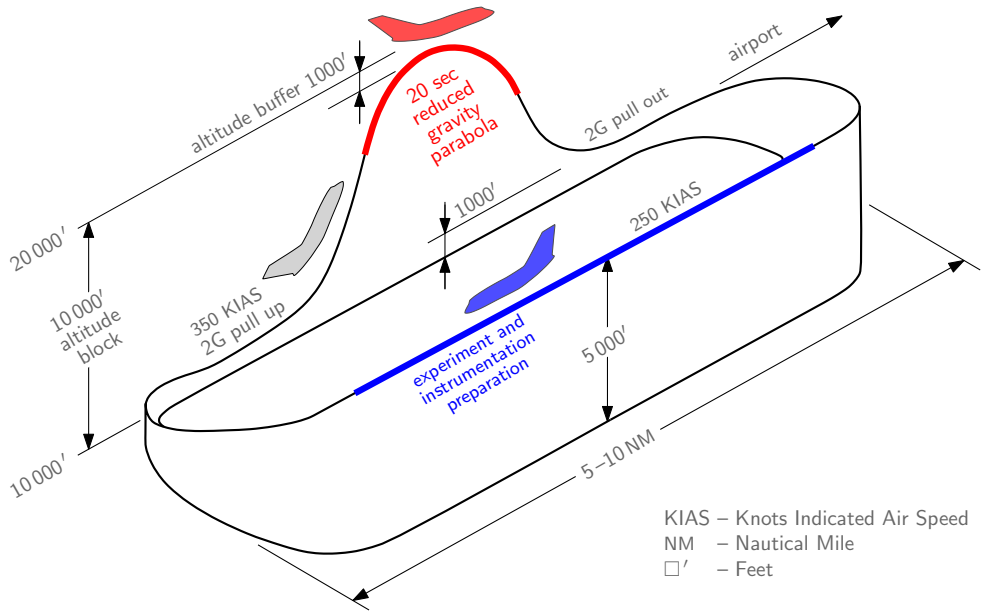

Figure 2: Elements of a typical reduced-gravity flight trajectory, including a reduced-g parabola as well as an experiment and instrumentation preparation phase between successive parabolas. The figure was reproduced based on reference [5].

tomated and rapid which makes it possible to increase the number of reduced-gravity parabolas that can be flown within a fixed flight campaign with soil consistently prepared before each and every parabola.

2.3 Control parameters

In the experimental campaign, the parameters of slip, wheel normal load and gravity were varied to investigate their influence on the wheel-soil interaction and rover wheel mobility performance.

To investigate the influence of each control parameter, the wheel loading and slip ratio were varied between $164\,\mathrm{N}$ to $225\,\mathrm{N}$ and 10% to 70%, respectively. From this extensive database, in the present study we consider only the the 70% slip data with $164\,\mathrm{N}$ load applied on the ground for comparing the results with different levels of gravity. This dataset was chosen as it has the most reliably detected velocity fields across all the gravity levels.

3 Extracting wheel-soil interaction parameters from visualization

The modified terramechanics model presented in this work requires an effective radius, R, and the average soil velocity near the wheel rim, $\bar{v}$. These parameters are extracted from analyzing visualization results based on the experimental data, as will be described in this section.

3.1 Camera setup

The ExoMars wheel prototype is placed tightly against the glass window without any forcing to maintain a low friction interface. A high-speed camera with a 16 mm EFL f/1.4 lens is used to capture images of the soil in the region where it interfaces with the wheel. There is limited space in the cabin to capture the view directly during the reduced gravity flights, thus, the camera points downward and views the region of interest through an angled mirror. The view angle of the camera and the field of view of the glass sidewall are shown in orange in Fig. 1. The camera is attached to the horizontal axis and moves alongside the wheel capturing high-resolution images from the mirror reflection of the soil and the wheel. The depth of the soil visible extends about 160 mm below the undisturbed soil surface.

Two external LED flood lights are placed approximately 1000 mm apart at both ends of the mirror at an angle pointing towards it, to avoid direct reflection into the camera, providing illumination, high contrast, and reduced shadows along the mirror.

The ES-2 soil simulant utilized in this study is a white (nearly featureless) fine aeolian sand with grain sizes in the range of 30-100 μm [4]. This is a challenging soil to analyze with computer vision but, as will be shown, it was achieved successfully. A raw image from the testbed with the soil is shown in Fig. 3, with indications of the direction of the motion of the wheel. The wheel is driving counter-clockwise and it travels from right to left of the image. The snapshots in Fig. 4 show the wheel as it is advancing, deforming and sinking into the soil while it rotates between two subsequent “midway-between-springs” contact configurations. The change in contact angles, the detection of the effective contact patch, and the effect of grousers are discussed in the next sections.

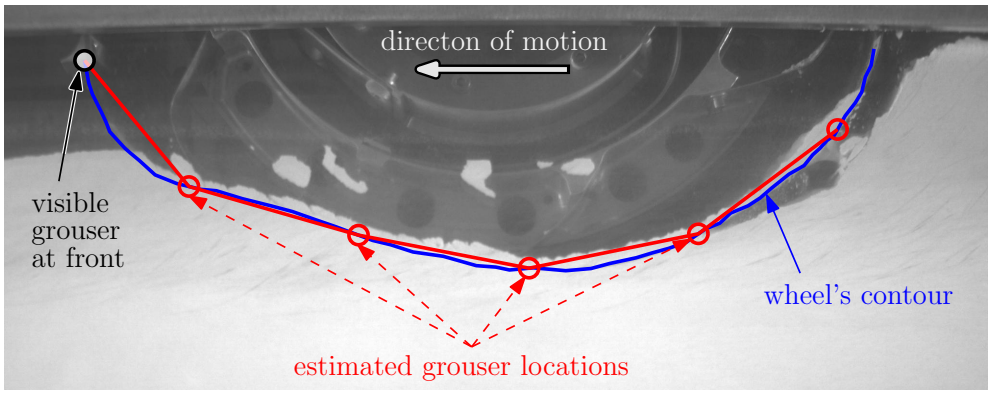

Figure 3: Image captured through the glass window of the ExoMars flexible wheel in ES-2 Martian simulant; note camera field of view shown in Fig. 1. This image shows the interface contact patch of the flexible wheel with soil at 70% Slip and 164N wheel loading under Martian gravity. The locations of grousers are estimated based on the arc length of the wheel's contour.

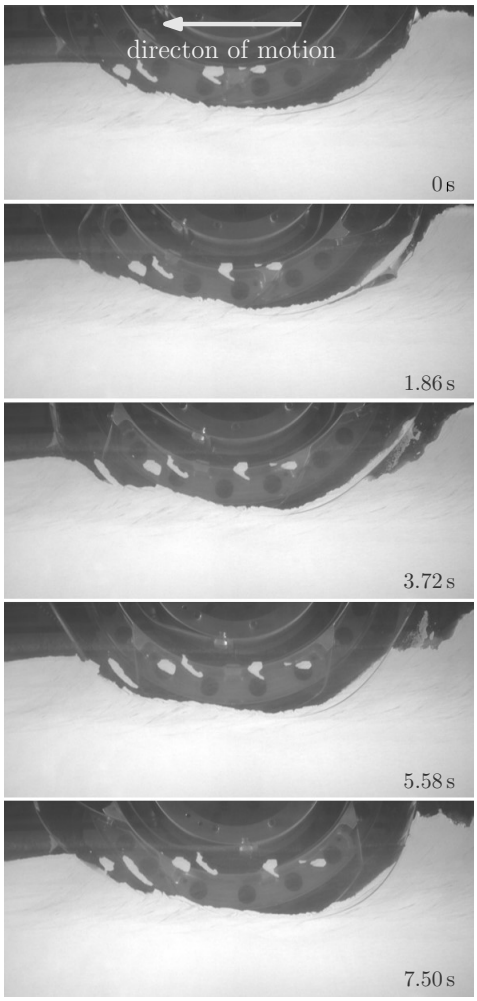

Figure 4: Snapshots of the flexible wheel as it turns and advances under Martian gravity at 70% slip and 164 N vertical load. The snapshots were taken 70 frames ($70/37.7 \approx 1.86$ s) apart, and it took 7.5 seconds for the wheel to rotate between two subsequent "midway-between-spring" contact configurations.

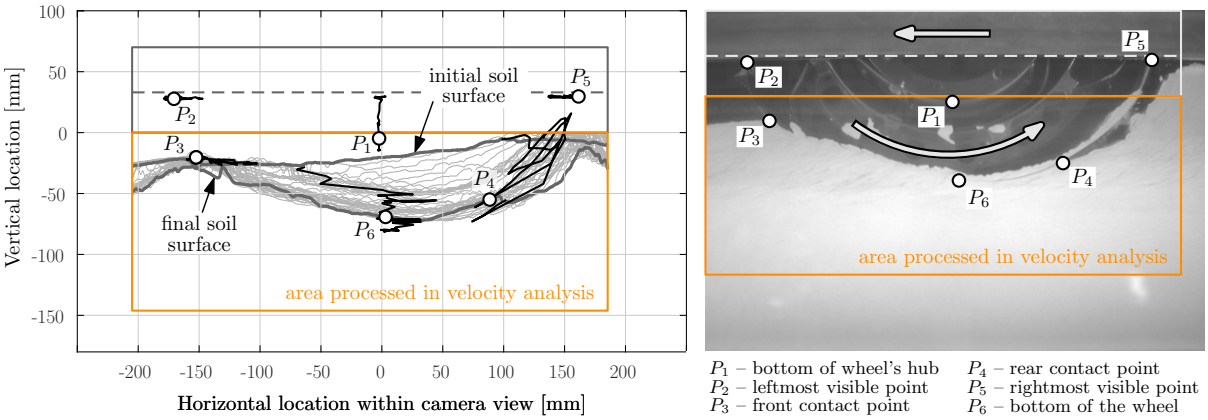

Figure 5: Contact patch and sinkage of the flexible ExoMars wheel

3.2 Effective radius from surrogate wheel model

The explicit consideration of wheel flexibility significantly increases the complexity of the model and can be computationally expensive. Therefore, often rigid surrogate models are used to capture the global effect of wheel flexibility on the contact patch. By referring to earlier experimental evidence [3] suggests the use of a larger diameter wheel which simply replaces the original geometry between the front and rear contact points. An iterative method is described in [23] to determine this diameter as a function of the tire stiffness and pressure. The contact patch is often decomposed into a front circular segment and a flat rear part that carries most of the vertical load [24]. The model presented in [10] uses an ellipse instead of the circular segment and also considers the elastic rebound of the soil towards the end of the contact patch. Other reported work includes parabolic [23] or exponential [15] approximations. Once the contact patch is described, these surrogate wheel models can be used to calculate the wheel-soil interaction forces based on terramechanics approaches developed for rigid wheels.

The goal of this subsection is to identify the effective radius of a compliant wheel that has flattened out due to loading. For this, we do not adopt the above analytical methods to determine the diameter of the surrogate wheel. Instead, the diameter is directly obtained from the experimental data through image processing. This makes it possible to carry out a non-steady state analysis and properly take into account the variation in the contact length and angles due to non-uniform radial stiffness.

3.2.1 Contact patch

The wheel-soil interface is shown in Fig. 3. The chosen image was taken during the Martian gravity experiment at 70% slip with $164\,\mathrm{N}$ loading, but similar contact geometries were observed throughout all the experiments. It can be seen that the grousers transfer the soil backwards and the soil forms a deposit behind the wheel (see also Fig. 4). The contact patch has a short curvilinear segment at the beginning followed by a flat part and another curvilinear segment at the end. For the sake of simplicity, here, a circular arc is considered instead, which is sufficiently accurate for the purpose of the present analysis.

In order to detect the wheel-soil interface the darker (low intensity) pixels of the gray-scale video frames were removed by image thresholding. As a result, the binary image of the soil was isolated. The segment that represent the contact patch was found by manually selecting the front and rear contact points (see P_3 and P_4 in Fig. 5). Then, the diameter of the surrogate wheel model was determined by fitting a circle for the corresponding segment of the contact patch using Taubin's method [29]. The model fitted to the image shown in Fig. 3 is presented in Fig. 6, where x_C and y_C are the coordinates of the centre of the fitted circle measured from the middle of the frame and the undisturbed soil surface, R is the effective radius, and θ_f and θ_r denote the front and rear contact angles, respectively. The contact length depends on the flexibility of the wheel and the applied load. According to our observations, on a rigid flat ground, either 2 or 3 grousers can be simultaneously in contact with the ground, which gives a 75-150 mm range for the variation of the contact length. This can significantly increase in sandy soil where the actual soil flow under the wheel is influenced by the grousers and the different gravity conditions (see the estimated grouser locations in Fig. 3).

3.2.2 Effects of gravity and wheel flexibility

The ExoMars wheel (see Fig. 1) used in this research has flexible loops and leaf springs that help to maximize to contact area under the wheel. This reduces the sinkage of the wheel and therefore the compaction resistance is also lowered. On the other hand, the flexible elements cause a complex radial stiffness distribution along the circumference of the wheel. There are three layers (looking along the wheel axis) each containing three loops and the middle layer is rotated by 60 degrees relative to the other two. As a consequence, the stiffness peaks six times in one full rotation of the wheel. This may be seen as if there were six "virtual spokes"

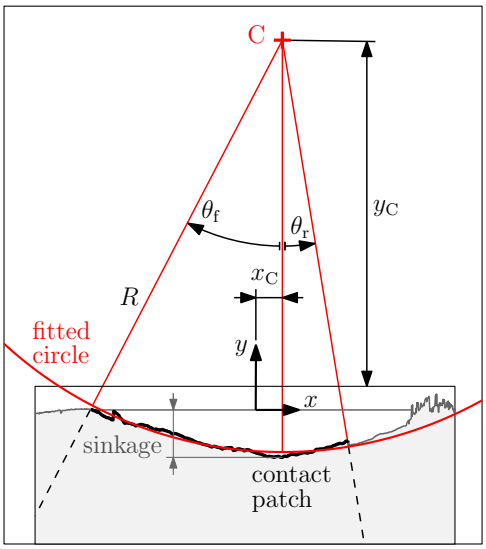

Figure 6: Surrogate (rigid body) wheel model

strengthening the flexible wheel and reducing its effective radius locally. At larger sinkage values there is also a periodic build up of torsional energy as a bulge tends to form near the front contact point (see Fig. 4). When this energy is released the contact patch flattens and the effective radius increases. In Fig. 5 it can be seen that the front and rear contact points move back and forth horizontally relative to the wheel's hub. The three visible periods correspond to the number of "virtual spokes" that passed by during the experiment[1].

The periodic change of the effective radius, R, relative to the nominal radius, r, is also shown in Fig. 7 at three different gravity levels. In the second part of the experiments (closer to the desired steady state) the fitted radius slightly decreases with gravity. This shows that the bearing capacity of the soil is lower and the deformation of the wheel is somewhat smaller. This effect is more clear when one compares the Lunar and OGE results. The upper charts show that the surrogate wheel model is well centred horizontally and the change of the effective radius is mostly reflected in the change of the vertical offset of its centre.

[1]The rim speed of the wheel was fixed at $r\omega = 20\,\text{mm/s}$ and its perimeter is $2r\pi \approx 895\,\text{mm}$. The experiment lasted about 22 seconds leaving half a turn for the wheel, and therefore 3 virtual spokes could pass over the contact patch.

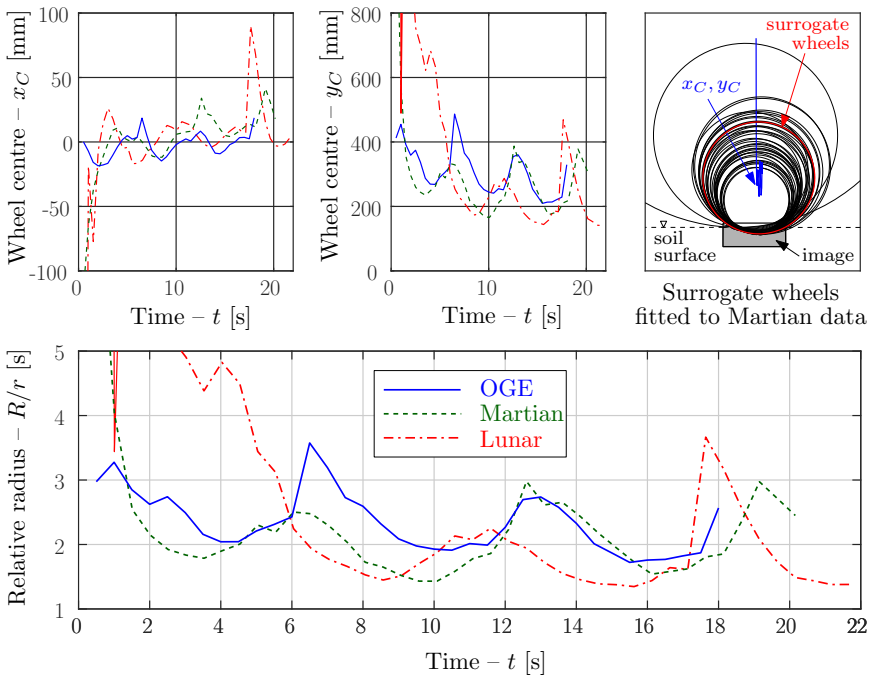

Figure 7: Comparison of surrogate wheel parameters over time and across different gravity levels

3.3 Velocity field analysis

The high-speed camera recordings were analyzed using the Soil Optical Flow Technique (SOFT) [25] which obtains the horizontal and vertical velocity components of soil particles by processing subsequent images; preliminary visual results were reported in reference [20]. A primary goal of this subsection is to identify the average soil velocity near the wheel rim[2] which can be used to estimate the loss of traction due to the different mobilization of the soil at different gravity levels. In addition the presented analysis is intended to show the effect of grousers and support the considerations taken during the subsequent dynamics modelling.

As it was discussed earlier in Section 3, the used soil simulant has no distinct features and its average grain size is very small. This made the detection of the velocity field difficult by using SOFT. Therefore, for the velocity field analysis below, we consider averaged data of about 0.5 seconds[3]. The averaged period is sufficiently long for reducing noise, while it still gives a good temporal resolution.

[2]Unless otherwise specified, near the wheel rim velocity means the average velocity of soil particles at a distance from zero to the height of grousers from the surface of the detected surrogate wheel.

[3]The OGE experiments were recorded with 8fps, while the Martian and Lunar experiments had a higher, 37.7 fps, frame rate. Therefore 5 and 20 frames had to be averaged, respectively.

The classical terramechanics interaction models rely on the wheel kinematics and neglect the soil motion under driven wheels [33, 3]. The elastoplastic formulation proposed in [2] also uses the velocity distribution of a rigid wheel, but it assumes that the soil velocity can be approximated by exponentially decaying the contact patch velocity components along the radial direction. This assumption is physically sound and can give a basis for quantifying the effect of gravity as a decreasing rate of decaying is expected at lower gravity levels.

In order to quantify the effect of gravity on the soil velocities, as a first step, the horizontal and vertical velocity field components were obtained, and by using the surrogate wheel model the velocity field was transformed into polar form. This is illustrated in Fig. 8, where a 70% slip data set with $164\,\mathrm{N}$ loading is considered under Martian gravity. The colorbars have units of mm/s. During the experiments the rim speed was kept at $r\omega = 20\,\mathrm{mm/s}$ and the linear velocity of the wheel at 70% slip was $v_x = 6\,\mathrm{mm/s}$. By assuming constant sinkage the tangential and normal velocity components can be expressed as $v_t = -v_x \cos\theta - r\omega$ and $v_n = v_x \sin\theta$, respectively, which predicts that the tangential velocity should be around 14mm/s in magnitude and the normal velocity needs to be between -6 and 6 mm/s for the limited range of the contact angle. This is in agreement with the experiments.

The rigid body velocity profile and the actual soil velocity near the rim are compared in Fig. 9 in more detail. In this figure the grey lines show the velocity profiles near the rim at different depths between 0 and $8\,\mathrm{mm}$. The red curves are the averages of these, while the solid black lines represent the rigid body predictions. The tangential component increases from the zero velocity of the undisturbed soil to approach the predicted value of -14 mm/s at the bottom of the wheel. The grousers accelerate the soil under the wheel and they have an important effect on the shape of the velocity profile. In the figure the approximate grouser locations (see Fig. 3) are shown as vertical dashed lines. The tangential soil velocity increases ahead (to the right) of these as the grousers push the soil forward (from left to right), while there is a slowdown behind the grousers (to the left of the dashed lines) due to the upward flow which replaces the transported soil. The upward soil flow can be seen as negative values in case of the normal velocity distribution. The results show that rigid body velocity profile can be used to predict the velocity of the topmost soil layer, but the grouser can significantly change the velocities locally. Also the figures show that in the usual range of contact angles the sine and cosine functions in the rigid wheel formulas could simply be replaced by a linear and a constant term, respectively.

The average tangential velocity and the root-mean-square (RMS) normal velocity was used

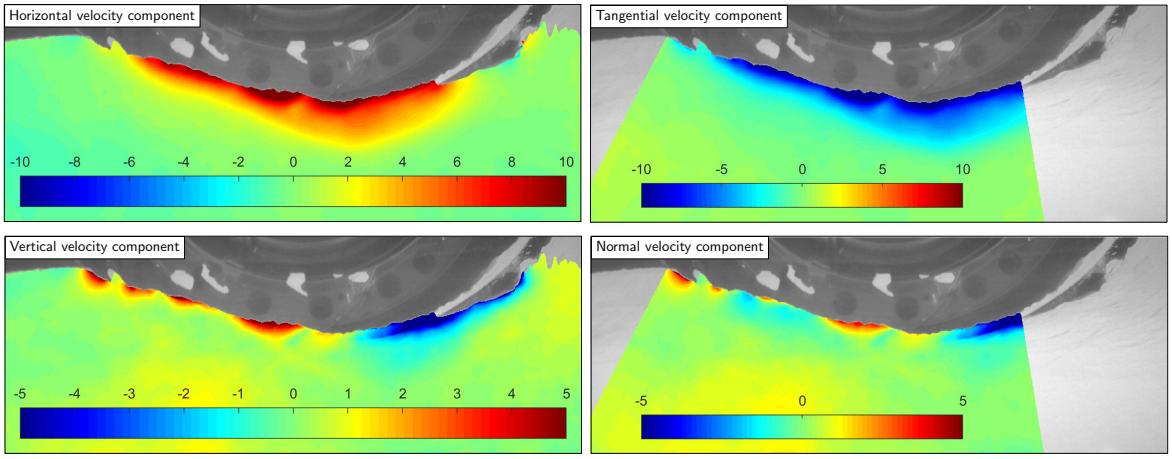

Figure 8: Cartesian (left) and polar (right) velocity component fields

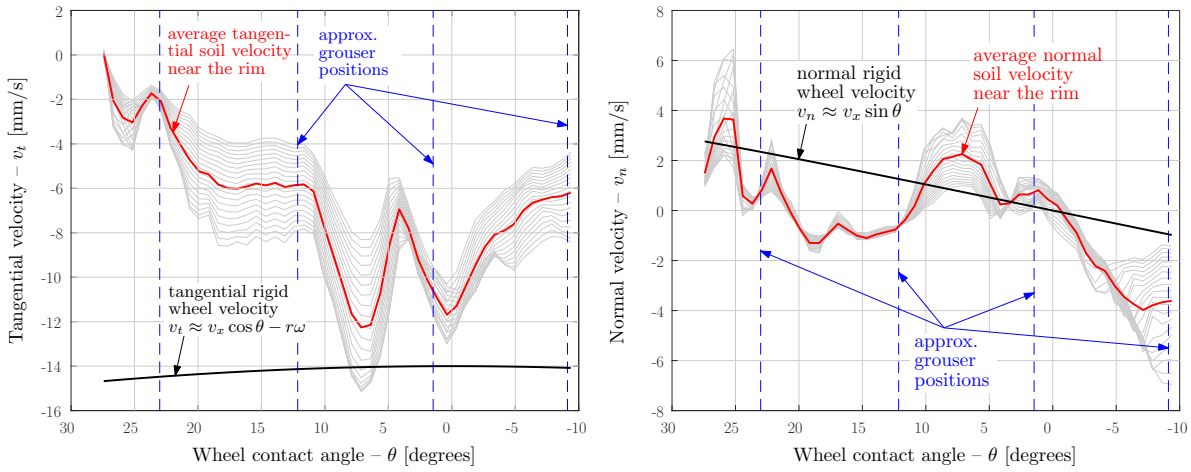

Figure 9: Tangential (left) and normal (left) soil velocity distribution along the rim of the wheel

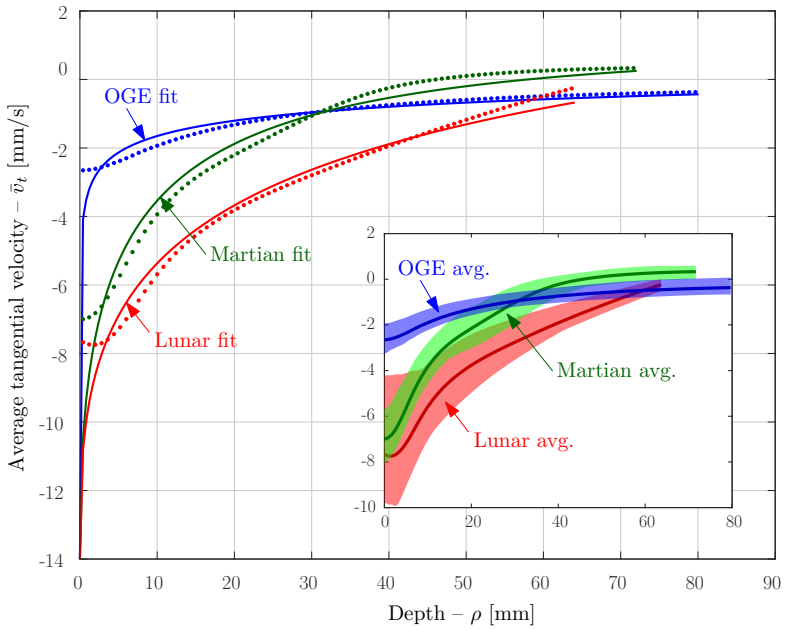

Figure 10: Decaying of the tangential velocity component with depth

to characterize the decaying of the corresponding velocity fields. These are shown in Figs. 10 and 11, where, in order to eliminate the initial transients, only the second half of the experiments were considered. The shaded areas represent the results obtained in 20 different averaged velocity field data of 0.5s duration. The average of these, shown as the thick center lines, were used for the curve fitting.

Based on Fig. 11, the decaying of the normal velocity component may be described by the simple exponential expression

$$v_n(\rho) = a_1 \exp(-a_2 \rho) + a_3 \tag{1}$$

where $\rho = R - r$ and $a_i, i = 1, 2, 3$ are the fitting parameters. The non-zero value of a_3 is due to the noisy velocity detection of the featureless powdery soil simulant.

The tangential velocity components have a similar, but not directly exponential characteristics. The exponential decaying in this case can be described in the form

$$v_t(\rho) = (b_1 - v_t^*) \exp(-b_2 \rho^{b_3}) - b_1 \tag{2}$$

where v_t^* is the magnitude of the rigid body reference velocity, and $b_i, i = 1, 2, 3$ are fitting parameters. The reference velocity is chosen as the tangential rigid body velocity at the bottom

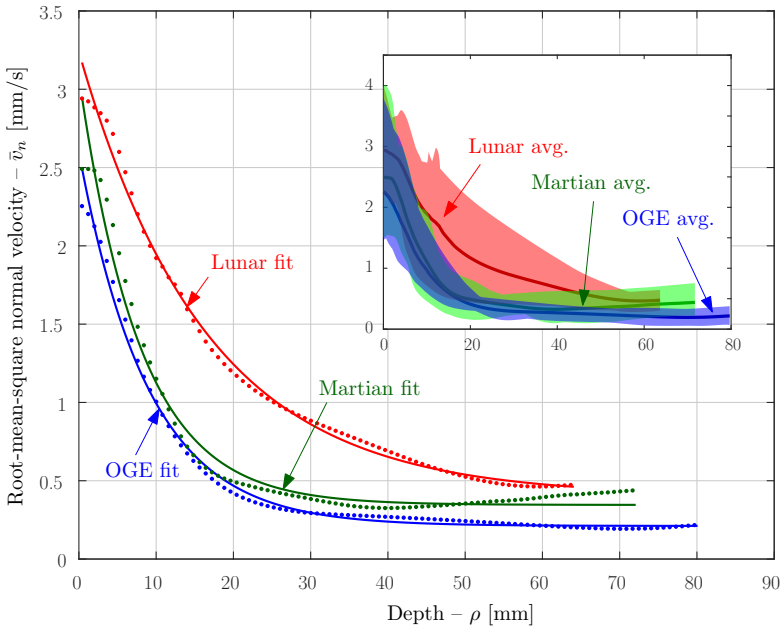

Figure 11: Decaying of the normal velocity component with depth

Table 1: Velocity field fitting parameters

	a_1 [mm/s]	a_2 [mm^{-1}]	a_3 [mm/s]	b_1 [mm/s]	b_2 [mm^{-1}]	b_3 [$-$]
OGE	2.388	0.1114	0.2113	-1	1.238	0.1461
Martian	2.737	0.1255	0.3456	-1	0.4093	0.4655
Lunar	2.835	0.0608	0.4036	-5	0.2572	0.372

of the wheel ($v_t^* = -14\,\text{mm/s}$). Similarly as above, parameter b_1 compensates for the noise in the experimental data. The estimation of the camera velocity can be seen as another possible source of the constant error at larger depth values. The fitting parameters used in Eqs. (1) and (2) are summarized in Table 1.

The results show that the tangential velocity of the soil along the rim clearly increases with the decreasing gravity levels. Consequently, the relative velocity between the wheel and the soil is decreasing which results in lower shear displacement and traction. The effect of gravity on the normal components is less visible. The OGE and Martian results are quite similar, but in the Lunar case the decaying of the normal component is substantially slower. This indicates more sinkage which is in agreement with the experimental observations. Note that, as opposed to the experiments reported in [16], here the external force applied through pneumatic cylinders was increased to compensate for the weight loss of the wheel at different gravity levels. This way all the experiments were carried out with the same overall vertical load that includes both the applied external force and the gravity force. This explains the increasing sinkage at decreasing

gravity levels.

4 Dynamics model

Focusing on the accurate prediction of the draw-bar pull of a wheel, this section presents the main modelling elements necessary for capturing the dynamics of the wheel operating on soft soil under different gravity levels. First, the wheel soil interaction model is discussed considering the effect of gravity and slip sinkage. Then, a simulation study is presented to compare the predicted draw-bar pull to experimental results.

4.1 Wheel-soil interaction

In terramechanics analysis, the pressure-sinkage relationship serves as a basis for calculating the normal and tangential stress distributions under the wheel. In its original form the empirical formula published in [3], which relies on the assumption of quasi static loading, does not reflect the effect of gravity. A modification was proposed in [31] where the gravitational acceleration was factored out explicitly. This modification is based on the observation of Reece, who showed the link between the bearing capacity theory of soils and the empirical pressure sinkage formula in [21]. These different forms of the pressure-sinkage formula are shown below

$$\sigma = (k_c/b + k_\phi) z^n \quad \rightarrow \quad \sigma = \left(\underbrace{ck'_c}_{k_1} + \underbrace{\gamma b k'_\phi}_{k_2 b} \right) \left(\frac{z}{b}\right)^n \quad \rightarrow \quad \sigma = \left(\frac{ck'_c}{b^n} + \frac{\gamma_m k'_\phi}{b^{n-1}} g \right) z^n \tag{3}$$

where σ is the normal stress (pressure) under the wheel and z denotes the sinkage. In addition, parameters c, γ and γ_m are the cohesion, the specific weight and the specific mass (or bulk density) of the soil, respectively, and k_c, k_ϕ and n are experimentally identified pressure sinkage constants obtained by curve fitting. The primed symbols denote dimensionless quantities, b is the characteristic dimension of the contact patch, and g is the gravitational acceleration. In [32], the factor multiplying gravity was combined into a single parameter $K_\phi = \gamma_m k'_\phi / b^{n-1}$ which was considered as constant at different gravity levels. Similarly, the term due to cohesion can be written as $K_c = ck'_c/b^n$. Although there is no experimental evidence supporting this assumption, it appeared to be valid throughout the examples presented in [32]. Therefore, in the following

we adopt the same assumption.

In case of flexible wheels the deformation of the wheel results in a larger contact area, and therefore the contact pressure drops. This effect is modelled implicitly by Eq. (3) as the sinkage associated with a surrogate wheel with larger radius is smaller.

There are however important dynamic effects that the pressure sinkage formulas cannot model and may become relevant in certain cases. This is due to the quasi static character of such wheel-soil interaction models. They do not include time dependence. Another shortcoming of the quasi-static assumption is that these equations predict the same pressure distribution for different wheel slips. The difference between the predicted pressure and the experimentally observed one can be significant at high slip values. The increased sinkage at higher slip values was studied empirically by Ding et al. in a series of publications [9, 8, 7, 6]. In these papers the slip sinkage phenomenon is captured by applying different slip-dependent sinkage coefficients in the pressure sinkage equations. For different operating conditions and wheel types, different formulas were proposed in the form of linear, quadratic or even rational polynomial expressions for the sinkage exponent. In this paper, we assume the linear relationship in the form of

$$\sigma = (K_c + K_\phi g) z^{n_0 + n_1 i_d} \tag{4}$$

where $i_d = 1 - v/(r\omega)$ is the slip for driving conditions with v and ω being the linear and angular velocities of a wheel with radius r [4], and $n = n_0 + n_1 i_d$ is the slip dependent sinkage exponent. The simulation study presented in the next sections uses values for n_0 and n_1 proposed in [8] for a wheel with similar geometry to the ExoMars wheel prototype. It has to be noted that these empirical parameters may depend also on the level of gravity; this possible dependence is not considered. An alternate, simple analytical slip-sinkage model was also proposed in [18] in the form $z = K_{ss} z_0$, where z_0 is the sinkage associated with the original pressure sinkage equations and $K_{ss} = (1 + i_d)/(1 - 0.5 i_d)$ is a slip dependent multiplier in the range of $1 < K_{ss} < 4$. For further possible models, comparison, and application notes the interested reader is referred to [11]. It is also noted that in cohesive soils the sinkage may be independent of the slip [12].

[4] r is the original (undeformed) wheel radius; for a flexible wheel (such as ExoMars) if there is a significant deflection along the traverse, there is uncertainty in finding the appropriate radius and calculating the precise slip at any given moment. However, despite the deflection the circumference of the rim does not change (it is steel sheet metal) and over a long enough rotation, the total length of rim rotating past has to approach the arc lenght corresponding to the original radius or the wheel would come apart. Thus, i_d, even allowing for wheel deformation, gives the correct slip on average.

The grouser configuration of the wheel can also have significant effect on the wheel sinkage and on its tractive performance. For wheel design, [28, 27, 14] gives useful instructions, while for modeling the effect of grousers [6] proposes an expression for the minimum necessary lug/grouser height that determines whether the individual effect of the grousers needs to be considered or their cumulative effect can be modelled using an increased effective radius. According to reference [6], this effective shearing radius may be defined as $R_e = R + c_g h_g$, where R is the radius of the wheel (or that of the surrogate model), h_g is the height of the grousers, and coefficient c_g describes the efficiency of the grousers. This coefficient depends on the radius of the wheel, the number and height of the grousers, and also on the internal friction of the soil [9].

It has to be noted that considering an enlarged shearing radius also increases the front and rear contact angles (see Fig. 6) used for calculating the shear deformation, and ultimately the draw-bar pull of the wheel. In the following θ_f' denotes the increased front contact angle and the rear exit angle is considered in the form $\theta_\mathrm{r} = c_3\theta_\mathrm{f}$ with c_3 being a constant parameter. For the sake of simplicity, in this study we also keep the location of the maximum normal stress, $\theta_\mathrm{m} = c_1 + c_2 i_d$, independent of the gravity.

With these considerations the calculation of the normal stresses can be done by using the Wong-Reece model [33]. The important generalizations here include the consideration of the slip sinkage [8] and the flexibility effects. By also including the effect of gravity the normal stress distribution along the contact patch is given by

$$\sigma(\theta) = \begin{cases} (K_c + K_\phi g) z^{n_0+n_1 i_d} (\cos\theta - \cos\theta_\mathrm{f})^{n_0+n_1 i_d} & \theta_\mathrm{m} \le \theta \le \theta_\mathrm{f} \\ (K_c + K_\phi g) z^{n_0+n_1 i_d} \left(\cos\left(\theta_\mathrm{f} - \dfrac{\theta_\mathrm{f} - \theta_\mathrm{m}}{\theta_\mathrm{m} - \theta_\mathrm{r}}(\theta - \theta_\mathrm{r})\right) - \cos\theta_\mathrm{f}\right)^{n_0+n_1 i_d} & \theta_\mathrm{r} \le \theta \le \theta_\mathrm{m} \end{cases} \tag{5}$$

where the front contact angle is computed as $\theta_\mathrm{f} = \arccos(z/R)$ by using the radius of the surrogate wheel model.

Then the shear stress distribution may be determined by employing he Janosi-Hamamoto formula [30] in the form

$$\tau(\theta) = (c + \tan\phi)(1 - \mathrm{e}^{-j/K}) \tag{6}$$

where the shear deformation is calculated along the shear surface with the effective radius

$R_e = R + c_g h_g$ and front contact angle $\theta'_{\mathrm{f}} = \arccos(z/R_e)$ as

$$j(\theta) = R_e\big(\theta'_{\mathrm{f}} - \theta - (1 - i_d)(\sin\theta'_{\mathrm{f}} - \sin\theta)\big) \tag{7}$$

The shear deformation calculated above is based on the assumption of steady state motion and on the top of that the relative shearing velocity is taken as if the soil was not moving under the wheel. In reality, as it was shown earlier, the average soil velocity along the contact patch can change significantly at different gravity levels. When this becomes important, the shear deformation should be calculated as

$$j(\theta) = R_e\big((\theta'_{\mathrm{f}} - \theta)(1 - \bar{v}/\omega) - (1 - i_d)(\sin\theta'_{\mathrm{f}} - \sin\theta)\big) \tag{8}$$

where $\bar{v}$ and ω are the average soil velocity near the wheel and the angular velocity of the wheel, respectively. At lower gravity levels $\bar{v}$ increases, which reduces the shear deformation and therefore the tractive performance of the wheel. This novel formula was derived by integrating the shear velocity along the contact patch, by considering its reduction due to the soil motion characterized by the average soil velocity.

The distributed force system acting at the wheel-soil interface can be resolved about the centre of the surrogate wheel for simulation purposes. The resultant normal and tangential force components as well as the resistance torque of the soil can be expressed as

$$F_{\mathrm{C}x} = F_{\tau x} + F_{\sigma x} = R_e b \int_{\theta_{\mathrm{r}}}^{\theta_{\mathrm{f}}} \tau\cos\theta\,\mathrm{d}\theta - Rb\int_{\theta_{\mathrm{r}}}^{\theta_{\mathrm{f}}} \sigma\sin\theta\,\mathrm{d}\theta \tag{9}$$

$$F_{\mathrm{C}y} = F_{\tau y} + F_{\sigma y} = R_e b \int_{\theta_{\mathrm{r}}}^{\theta_{\mathrm{f}}} \tau\sin\theta\,\mathrm{d}\theta + Rb\int_{\theta_{\mathrm{r}}}^{\theta_{\mathrm{f}}} \sigma\cos\theta\,\mathrm{d}\theta \tag{10}$$

$$T_{\mathrm{C}z} = T_{\tau z} = -R_e^2 b \int_{\theta_{\mathrm{r}}}^{\theta_{\mathrm{f}}} \tau\,\mathrm{d}\theta \tag{11}$$

where point C is the centre of the surrogate rigid wheel, x is direction of forward motion, and direction y is normal to the ground. Here, similarly to [8], the effective shearing radius R_e is considered for calculating the contribution of the shear stress, while the slightly smaller surrogate wheel radius R was used to calculate the contributions due to the normal stress.

4.2 Model of experimental device

In the experimental setup shown in Fig. 1 the wheel and its driving motor are part of the wheel assembly which is mounted on a linear actuator. This actuator and the motor are used together to provide constant steady state slip during a specific experiment. In addition, the wheel assembly also contains a force/torque sensor that provides feedback for regulating the vertical load on the wheel. At different gravity levels the weight loss of the wheel assembly was compensated. The dynamic effects of the applied slip control are negligible compared to wheel flexibility and the effect of gravity. Therefore, for modelling the experimental device, these controllers can be idealized and the slip control may be seen as a velocity constraint.

With these considerations, the dynamics of the wheel can be captured by using the surrogate rigid body model of the wheel (see Fig, 6) subjected to a slip constraint. The generalized forces acting on the wheel include the external load, F_v, the drawbar pull, F_p, the applied torque, T_a, the gravity force, mg, and the soil reactions given in Eqs. (9), (10) and (11). The points of application of these forces and their reduction to the original wheel centre are shown in Fig. 12. In the left free-body-diagram F_{Cx}, F_{Cy} and T_{Cz} are the soil reaction components calculated by using the surrogate wheel model but applied to the original wheel at a point coincident with the centre of the surrogate model. Another possible representation of the same set of forces is shown on the right, where $F_t = F_{\tau x}$ is interpreted as the traction force, and $F_c = -F_{\sigma x} = F_t - F_{Cx}$ is the magnitude of the compaction resistance force. In addition, the normal force simply becomes $F_n = F_{Cy}$ and, from the torque balance, the so-called residual resistance torque can be expressed as $T_{rr} = T_r + F_c\,\Delta y_{OC} - F_n\,\Delta x_{OC} - F_t(r + \Delta y_{OC})$, where $T_r = -T_{Cz}$ is the resistance torque obtained from the surrogate wheel model. By using these newly introduced forces, and considering the linear velocities, v_{Ox} and v_{Oy}, of the centre of the wheel together with its angular velocity, ω_z, as generalized velocities, the dynamic model of the *uncontrolled* experimental system can be formulated as

$$m\dot{v}_{Ox} = F_t - F_p - F_c \tag{12}$$

$$m\dot{v}_{Oy} = F_n - mg - F_v \tag{13}$$

$$I_z\dot{\omega}_z = T_a - T_{rr} - F_t r \tag{14}$$

where m and I_z are the mass and mass moment of inertia of the wheel, respectively.

In the conducted experiments the slip was controlled by keeping the rim velocity ($r\omega_z$) con-

stant. Therefore, considering a constant desired value for the angular velocity and also for the slip the following constraint relationships can be derived for the generalized velocities

$$u_1 = \omega_z - \omega_z^* = 0 \tag{15}$$

$$u_2 = (1 - i_d^*) r \omega_z - v_{Ox} = 0 \tag{16}$$

where ω_d^* and i_d^* are the desired values of the angular velocity and the associated driving slip.

For compactness, the above scalar equation may be rewritten in the matrix-vector form

$$\begin{bmatrix} \mathbf{M} & -\mathbf{A}^{\mathrm{T}} \\ \mathbf{A} & \mathbf{0} \end{bmatrix} \begin{bmatrix} \dot{\mathbf{v}} \\ \boldsymbol{\lambda} \end{bmatrix} = \begin{bmatrix} \mathbf{f} \\ -\alpha\, \mathbf{u} \end{bmatrix} \tag{17}$$

with

$$\mathbf{M} = \begin{bmatrix} m & 0 & 0 \\ 0 & m & 0 \\ 0 & 0 & I_z \end{bmatrix}, \quad \mathbf{A} = \begin{bmatrix} 0 & 0 & 1 \\ -1 & 0 & (1 - i_d^*) r \end{bmatrix},$$

$$\mathbf{v} = \begin{bmatrix} v_{Ox} \\ v_{Oy} \\ \omega_z \end{bmatrix}, \quad \mathbf{f} = \begin{bmatrix} F_t - F_p - F_c \\ F_n - mg - F_v \\ T_a - T_{rr} - F_t r \end{bmatrix}, \quad \mathbf{u} = \begin{bmatrix} u_1 \\ u_2 \end{bmatrix} \tag{18}$$

where $\mathbf{M}$ is the mass matrix, $\mathbf{A}$ is the Jacobian associated with the constraints collected in array $\mathbf{u}$, and $\mathbf{v}$ and $\mathbf{f}$ are the generalized velocities and forces, respectively. In addition, $\alpha \geq 0$ is a constraint stabilization parameter, and $\boldsymbol{\lambda}$ represent the constraint torque and force that are necessary to provide the desired slip.

For the numerical simulations the above model was complemented with a damping force in the vertical direction and also the vertical force was adjusted to compensate for the weight loss of the wheel at different gravity levels. Therefore, considering a constant load, e.g. $F_L = 164\,\mathrm{N}$ in the experiments, the vertical force in Eq. (17) can be expanded as $F_v = F_L - mg + b_z v_z$, where b_z is the coefficient of viscous damping modelling the dissipation of the ground. Although the introduction of the damping term seems arbitrary, it is physically meaningful and necessary as the quasi static wheel-soil interaction model in Eq. (3) cannot model physical dissipation. For handling numerical instabilities due to slow time integration rates in large systems reference

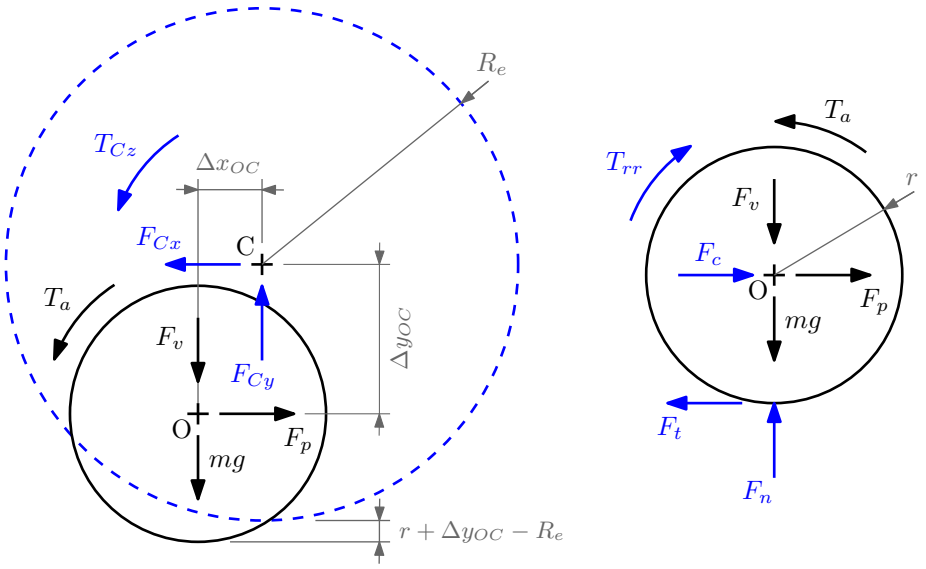

Figure 12: Application of forces on the wheel

[1] provides a robust, constraint-based method for modelling the soil interaction forces. In that work, the damping applied in the vertical direction is proportional to the instantaneous stiffness associated with the sinkage of the wheel. In the present model we consider a constant viscous damping only, and apply a sufficiently small (h=1 ms) integration time step to prevent numerical instabilities.

5 Comparison of simulation and experimental results

The dynamic simulation of the experimental system was carried out by using the equations derived in the previous section and the system parameters listed in Table 2. Among the wheel parameters, the mass m represents the total mass of the wheel assembly including the force sensor and the vertical column on which the wheel was installed; whereas the inertia I_z is an estimated value that corresponds to the wheel only. The provided soil density and internal friction angle correspond to the applied Martian engineering soil simulant ES2 [4], while others are estimated by using parameter values typical for loose sand [33, 30, 8]. Note, that k_c is neglected, and the value of k_ϕ was calculated by converting $k_2 = k_\phi b^{n-1}$ given in [33] in imperial units. This conversion uses a slightly different density (1360 kg/m^3) and n value (1.1504). As the parameters are from different sources they are not fully consistent with each other, but they all represent loose sand properties within a reasonable range. The sinkage exponents were

property	symbol	value	unit
wheel			
mass of wheel assembly	m	9.6	kg
inertia of the wheel	I_z	0.004	kg m^2
original wheel radius	r	142.5	mm
height of grousers	h_g	12.5	mm
width of the wheel	b	120	mm
soil			
pressure-sinkage constant	k_c	0	kN/m^{n+1}
pressure-sinkage constant	k_ϕ	747	kN/m^{n+2}
bulk density	γ_m	1450	kg/m^3
shear modulus	K	3.81	cm
sinkage exponent	n_0	0.93	–
sinkage exponent	n_1	0.54	–
internal friciton angle	ϕ	37	$^\circ$
cohesion	c	0.75	kPa
max. pressure coefficient	c_1	0.18	–
max. pressure coefficient	c_2	0.32	–
grouser height coefficient	c_g	1	–
damping coefficient	b_s	100	Ns/m
simulation			
desired slip	i_d	70	%
desired rim speed	$r\omega_d$	20	mm/s
vertical load	F_L	164	N
time step	h	1	ms
constraint stabilization coeff.	α	10	1/s

Table 2: Model and simulation parameters

selected to match those of a similar sized wheel reported in [8] and it is assumed that for the shear deformation calculation the total height of the grousers can be used.

Figures 13 and 14 compare the experimental results obtained under on Earth and Martian conditions to steady state simulation results. These simulations were conducted by considering an average effective radius, $R = 2r$, and an average contact angle ratio, $c_3 = 1$ (see Fig. 15). In both figures it can be seen that in steady state the drawbar pull (DBP) and the applied torque (T) oscillate. This is mainly due to the flexibility of the used ExoMars wheel. One can also observe that in the OGE case the sinkage stabilizes at an approximately steady state value after 17 s, while in the case of the Martian gravity there was not enough time during the experiments to reach the steady state. For the comparison below the last sinkage value is considered as the steady state value.

All the simulations were conducted with both the nominal wheel radius (r) and surrogate wheel radius (R) for comparison. In Fig. 13, $z_{st}()$ corresponds to static sinkage values that include the effect of gravity using Eq. (3), whereas $z()$ includes dynamic sinkage and gravity based on Eq. (4). DBP() is computed using Eq. (5) through Eq. (11), with the expression of $j(\theta)$ given by Eq. (7) nominally or Eq. (8) when $\bar{v}$ is specified (i.e., $DBP(R,\bar{v})$). It can be seen that the constant exponent sinkage models with different radii, see lines $z_{st}(r)$ and $z_{st}(R)$, significantly underestimate the experimentally observed sinkage values, and therefore the use of these models would result in an overestimated drawbar pull. When slip-sinkage is considered, the simulated sinkage values are closer to those of the experiments. Without taking into account the soil motion under the wheel, the best prediction of both the sinkage and wheel performance was achieved by using the effective radius and considering the phenomenon of slip-sinkage.

When in the simulations the effect of gravity is modelled by using Eq. (3), and the effect of the average velocity of the soil under the wheel is also considered by applying the new shear deformation formula in Eq. (8), the drawbar pull prediction can further be improved. The corresponding reduced drawbar pull values are labelled as DBP(R,$\bar{v}$) in the figures, where $\bar{v}$ is the average tangential velocity of the soil under the wheel near the tip of the grousers (see Fig. 10). In the current example, considering Martian gravity, the additional reduction of the drawbar pull due to the increased soil motion is about 8-10 percent. This is about the same as the reduction that follows from the application of Eq. (3) alone, and therefore it cannot be neglected.

Based on the experiments one can conclude that the lower gravity increases sinkage (when the load is kept constant) and operating the wheel under such conditions results in lower performance. The recent experiments also show that the flexibility of the wheel has an important effect on the achievable drawbar pull. In order to show that the large oscillations in the drawbar pull are due to wheel flexibility, a second simulation study was conducted using the OGE and Martian data, where both the variation in the effective radius and the contact angle ratio shown in Fig. 15 were considered. To model the fluctuation of these values a weighting function was constructed in the form

$$W(\theta, x_{\max} - x_{\min}, \nu, \theta_0) = 1 - \frac{x_{\max} - x_{\min}}{2\, x_{\max}} \big(1 + \tanh(\cos(\nu(\theta - \theta_0)))\big) \tag{19}$$

where $x_{\min}$, $x_{\max}$ are the minimum and maximum values of the quantity x which needs to be scaled along the circumference of the wheel with frequency ν and having a local maximum

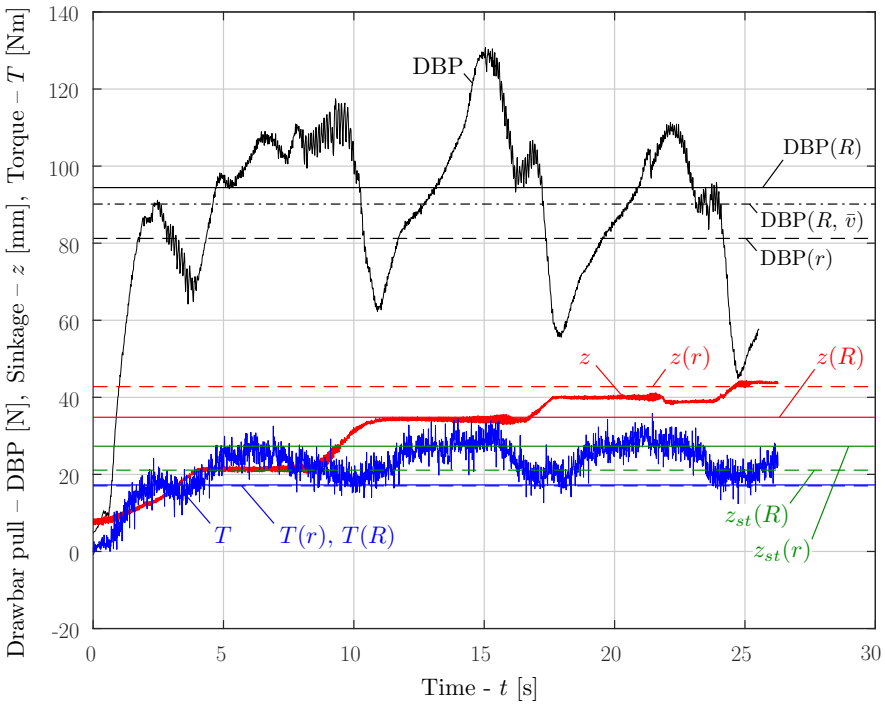

Figure 13: Comparison of steady state simulation results with experiments (OGE)

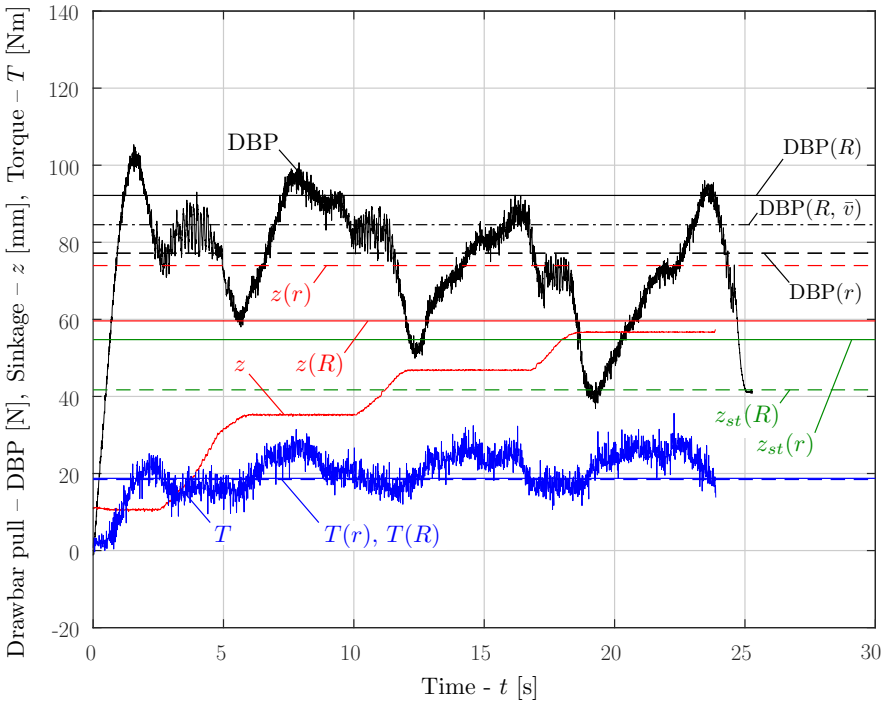

Figure 14: Comparison of steady state simulation results with experiments (Martian)

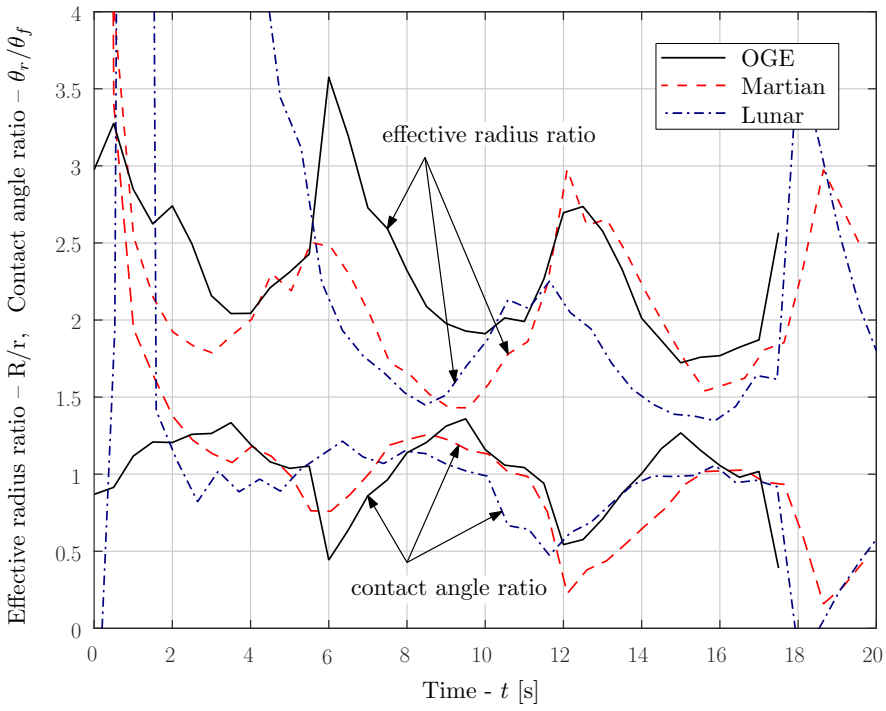

Figure 15: Fluctuations in surrogate wheel model parameters

at the initial angle θ_0. This scaling function is visualized in Fig. 16 for certain parameters. For modelling wheel flexibility under different gravity conditions in the different experiments the minimum and maximum values collected in Tab. 3 were used with frequency $\nu = 6$. This frequency follows from the construction of the wheel (see Fig. 1) as it has flexible loops which form 6 virtual spokes (there are 3 flexible loops on both sides of the wheel, plus there are 3 inner loops rotated by 60 degrees relative to these). The results obtained with the varying scaled effective radius, $R(\theta) = R_{\text{max}} W(\theta, R_{\text{max}} - R_{\text{min}}, \nu, 0)$, and the corresponding contact angle ratio, $c_3(\theta) = c_{3,\text{max}} W(\theta, c_{3,\text{max}} - c_{3,\text{min}}, \nu, 0)$, are shown in Figs. 17 and 18. These figures show that

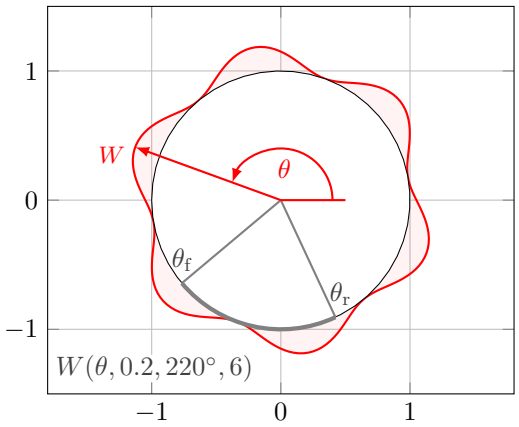

Figure 16: Visualization of the weighting function in Eq. (19)

	R_{min}	R_{max}	$c_{3,\text{min}}$	$c_{3,\text{min}}$
OGE	$1.7r$	$2.7r$	0.5	1.3
Martian	$1.5r$	$3r$	0.2	1.3
Lunar	$1.3r$	$3.5r$	-0.2	1.4

Table 3: Scaling limits used for flexible wheel modelling

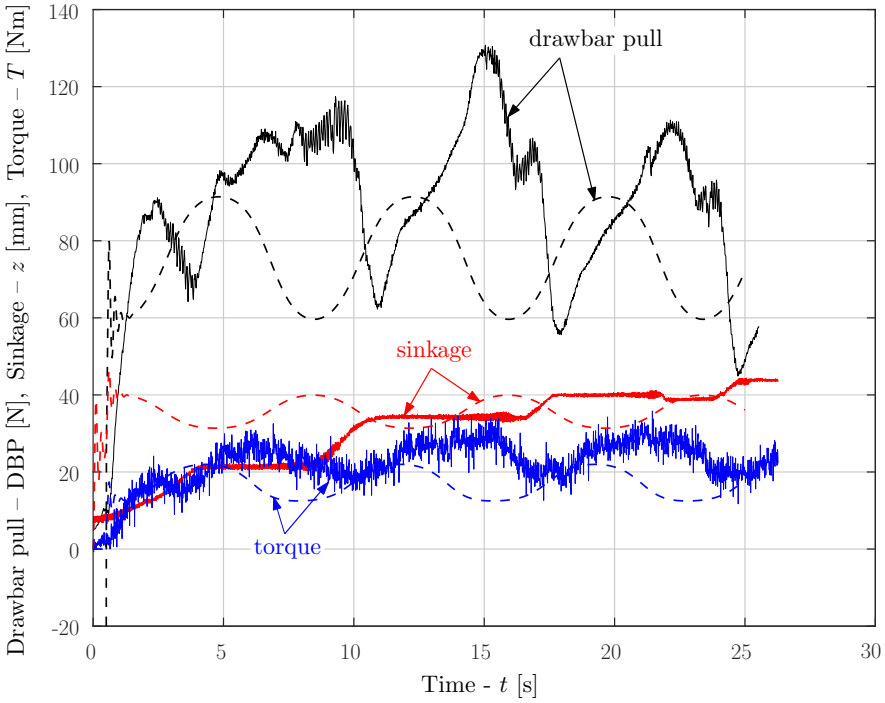

Figure 17: Effect of wheel flexibility (OGE)

the magnitude of the experimental drawbar pull oscillations are in good agreement with the simulation results obtained with the surrogate wheel model considering wheel flexibility. The applied torque values are also matching, while the simulated sinkage is quite different from the experimental values. This is because the simulated sinkages shown correspond to steady state operation. In case of the OGE comparison, the variation of the simulated sinkage is similar to that of the steady state values recorded in the second half of the experiment. The Martian simulation predicted slightly higher steady state oscillations in the sinkage than what was observed experimentally.

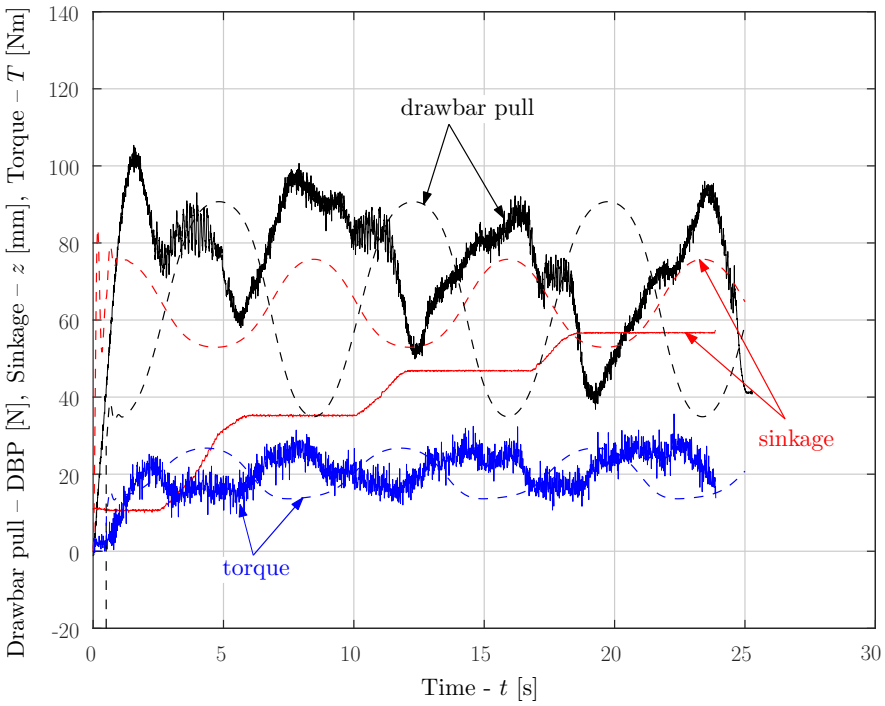

Figure 18: Effect of wheel flexibility (Martian)

6 Conclusion and future work

In this work, wheel-soil interaction modelling was investigated considering gravity effects and using experiments in both Earth and reduced-gravity conditions. The model proposed considers the slip-sinkage phenomenon and a surrogate modelling approach was used to take into effect the flexibility of the wheel. The third important feature of the model is the consideration of the soil motion under the wheel. For the calculation of the corresponding reduced traction force a new shear deformation formula was derived. The comparison of the simulation and experimental data show that the above extension of the gravity dependent slip-sinkage model can lead to a better prediction of the drawbar pull.

The analysis of experimental data showed that the contact patch of the flexible wheel varies periodically. The center of the fitted surrogate wheel circles stay approximately constant horizontally, but vary vertically with the periodically changing surrogate wheel radius. Furthermore, in the velocity field of the soil below the wheel, the decay of tangential velocity (as a function of radial distance into the soil away from the wheel rim) becomes more gradual with reducing gravity. The decay of normal velocity is slower in Lunar-g.

The effects of the flexible wheel (both in terms of the surrogate wheel radius to capture

wheel flattening, R, and a weighting/scaling function to capture periodically varying radial stiffness) and dynamic sinkage (i.e., slip sinkage) are important for correctly predicting sinkage and drawbar pull. Average soil velocity near the wheel, $\bar{v}$, should also not be ignored.

The presented reduced-gravity wheel-soil interaction modelling and data can also serve as a basis for developing new models. Future work will focus on determining the most appropriate soil velocity profiles for an elastoplastic formulation that inherently include the effect of slip-sinkage.

Acknowledgments

This project was undertaken with the financial support of the Canadian Space Agency. We would like to thank Canada's National Research Council Flight Research Laboratory for facilitating the parabolic flight campaign. We thank MDA for the loan of a prototype ExoMars rover wheel. F. González acknowledges the support of the Ministry of Economy of Spain through the Ramón y Cajal research program, no. RYC-2016-20222.

References

[1] Azimi, A., Holz, D., Kövecses, J., Angeles, J., Teichmann, M.: A multibody dynamics framework for simulation of rovers on soft terrain. Journal of Computational and Nonlinear Dynamics **10**(3), 031,004 (2015)

[2] Azimi, A., Kövecses, J., Angeles, J.: Wheel/soil interaction model for rover simulation and analysis using elastoplasticity theory. Transactions on Robotics **29**(5), 1271–1288 (2013)

[3] Bekker, M.G.: Theory of land locomotion: the mechanics of vehicle mobility. Ann Arbor, University of Michigan Press (1956)

[4] Brunskill, C., Patel, N., Gouache, T.P., Scott, G.P., Saaj, C.M., Matthews, M., Cui, L.: Characterisation of martian soil simulants for the ExoMars rover testbed. Journal of Terramechanics **48**(6), 419–438 (2011)

[5] CSA: Parabolic flights. http://www.asc-csa.gc.ca/eng/sciences/parabolic.asp (2018). [Online; accessed 12 December, 2018]

[6] Ding, L., Deng, Z., Gao, H., Tao, J.: Interaction mechanics model for rigid driving wheels of planetary rovers moving on sandy terrain with consideration of multiple physical effects. Journal of Field Robotics **32**(6), 827–859 (2015)

[7] Ding, L., Gao, H., Deng, Z., Nagatani, K., Yoshida, K.: Experimental study and analysis on driving wheels' performance for planetary exploration rovers moving in deformable soil. Journal of Terramechanics **48**, 27–45 (2011)

[8] Ding, L., Gao, H., Deng, Z., Tao, J.: Wheel slip-sinkage and its prediction model of lunar rover. Journal of Central South University of Technology **17**(1), 129–135 (2010)

[9] Ding, L., Gao, H., Deng, Z., Yoshida, K., Nagatani, K.: Slip ratio for lugged wheel of planetary rover in deformable soil: Definition and estimation. In: Proceedings of The 2009 IEEE/RSJ International Conference on Intelligent Robots and Systems. St. Louis, USA (October 11-15, 2009)

[10] Favedi, Y.: Prediction of tractive response for flexible wheels with application to planetary exploration rovers. Ph.D. thesis, University of Surrey, UK (2010)

[11] He, R., Sandu, C., Khan, A.K., Guthrie, A.G., Els, P.S., Hamersma, H.A.: Review of terramechanics models and their applicability to real-time applications. Journal of Terramechanics (2018). Https://doi.org/10.1016/j.jterra.2018.04.003

[12] Hegedus, E.: Pressure distribution and slip-sinkage relationship under driven rigid wheels. Tech. Rep. 8090, Land Locomotion Laboratory, Army Tank-Automotive Center, Warren, Michigan (1963). Http://www.dtic.mil/docs/citations/AD0695669

[13] Heverly, M., Matthews, J., Lin, J., Fuller, D., Maimone, M., Biesiadecki, J., Leichty, J.: Traverse performance characterization for the Mars Science Laboratory rover. Journal of Field Robotics **30**(6), 835–846 (2013)

[14] Inotsume, H., Moreland, S., Skonieczny, K., Wettergreen, D.: Parametric study and design guidelines for rigid wheels for planetary rovers. Journal of Terramechanics **85**, 39–57 (2019)

[15] Karafiath, L.L.: Soil-tire model for the analysis of off-road tire performance. Tech. Rep. RM-5411, Grumman Aerospace Corporation, Bethpage, New York, USA (1972)

[16] Kobayashi, T., Fujiwara, Y., Yamakawa, J., Yasufuku, N., Omine, K.: Mobility performance of a rigid wheel in low gravity environments. Journal of Terramechanics **47**(4), 261–274 (2010)

[17] Lindemann, R.A., Voorhees, C.J.: Mars exploration rover mobility assembly design, test and performance. In: Systems, Man and Cybernetics, 2005 IEEE International Conference on, vol. 1, pp. 450–455. IEEE (2005)

[18] Lyasko, M.: Slip sinkage effect in soil–vehicle mechanics. Journal of Terramechanics **47**, 21–31 (2010)

[19] McCoubrey, R., Smith, J., Cernusco, A., Durrant, S., Phillips, R., Jessen, S., Jones, H., Fulford, P.: ExoMars suspension and locomotion. In: Proceedings of the 12th International Symposium on Artificial Intelligence, Robotics and Automation in Space (i-SAIRAS 2014 (2014)

[20] Niksirat, P., Skonieczny, K., Nassiraei, A.A.F.: Characterizing the effects of reduced gravity on rover wheel-soil interactions using computer vision techniques. In: 2019 International Conference on Robotics and Automation (ICRA), pp. 4739–4745. Montreal, Quebec, Canada (May 20, 2019 - May 24, 2019)

[21] Onafeko, O., Reece, A.R.: Soil stresses and deformations beneath rigid wheels. Journal of Terramechanics **4**(1), 59–80 (1967)

[22] Patel, N., Slade, R., Clemmet, J.: The ExoMars rover locomotion subsystem. Journal of Terramechanics **47**(4), 227–242 (2010)

[23] Schmid, I.C.: Interaction of vehicle and terrain results from 10 years research at IKK. Journal of Terramechanics **32**(1), 3–26 (1995)

[24] Schwanghart, H.: Measurement of contact area, contact pressure and compaction under tires in soft soil. Journal of Terramechanics **28**(4), 309–318 (1991)

[25] Skonieczny, K., Moreland, S., Asnani, V., Creager, C., Inotsume, H., Wettergreen, D.: Visualizing and analyzing machine-soil interactions using computer vision. Journal of Field Robotics **31**(5), 820–836 (2014)

[26] Skonieczny, K., Niksirat, P., Forough Nassiraei, A.A.: Preparations for reduced gravity flights to examine ExoMars rover wheel-soil interactions. In: Proceedings of the 14th ESA Workshop on ASTRA, Noordwijk, Netherlands (2017)

[27] Skonieczny, K., Niksirat, P., Nassiraei, A.A.F.: Rapid automated soil preparation for testing planetary rover-soil interactions aboard reduced-gravity aircraft. Journal of Terramechanics **83**, 35–44 (2019)

[28] Sutoh, M., Yusa, J., Ito, T., Nagatani, K., Yoshida, K.: Traveling performance evaluation of planetary rovers on loose soil. Journal of Field Robotics **29**(4), 648–662 (2012)

[29] Taubin, G.: Estimation of planar curves, surfaces and nonplanar space curves defined by implicit equations with applications to edge and range image segmentation. IEEE Transactions on Pattern Analysis and Machine Intelligence **13**(11), 1115–1138 (1991)

[30] Wong, J.Y.: Theory of ground vehicles, 4th edn. John Wiley & Sons (2008)

[31] Wong, J.Y.: Predicting the performances of rigid rover wheels on extraterrestrial surfaces based on test results obtained on earth. Journal of Terramechanics **49**(1), 49–61 (2012)

[32] Wong, J.Y., Kobayashi, T.: Further study of the method of approach to testing the performance of extraterrestrial rovers/rover wheels on earth. Journal of Terramechanics (2012). Https://doi.org/10.1016/j.jterra.2012.10.004

[33] Wong, J.Y., Reece, A.R.: Prediction of rigid wheel performance based on the analysis of soil-wheel stresses, Part I. performance of driven rigid wheels. Journal of Terramechanics **4**(1), 81–98 (1967)